

Research Article

Phase Demodulation of Rotor Torsional Vibration Measurement under Time-Varying Speed

Moli Chen ¹, Nan Zheng ¹, Jun Zheng,² Zhu Jin,¹ and Guihuo Luo ¹

¹College of Energy and Power Engineering, Nanjing University of Aeronautics and Astronautics, Nanjing, Jiangsu, China

²Wuhu Diamond Aeroengine Co., Ltd., Wuhu, Anhui, China

Correspondence should be addressed to Moli Chen; chenmoli160@nuaa.edu.cn

Received 15 September 2021; Revised 17 January 2022; Accepted 17 February 2022; Published 11 April 2022

Academic Editor: Lei Hou

Copyright © 2022 Moli Chen et al. This is an open access article distributed under the Creative Commons Attribution License, which permits unrestricted use, distribution, and reproduction in any medium, provided the original work is properly cited.

When torsional vibration is measured with the zebra-tape method, the modulation signals can be contaminated by electrical noise, environmental noise, step noise, sensor nonlinearities, and so on. Although the amplitudes of these types of noise are very weak relative to the amplitude of the ideal pulse test signal, they may introduce large-scale random broad-spectrum noise to the signal phases. Such noise is difficult to remove using frequency domain, time-frequency-domain, or threshold sampling methods and seriously affects the accuracy of torsional vibration measurements. This paper presents a phase demodulation algorithm based on downsampling and local resampling (DSLRL) to improve the accuracy of torsional vibration measurements. To verify the proposed DSLRL algorithm, torsional vibration simulations and experiments are conducted under a time-varying rotation speed. The results show that the angular displacement signal obtained from the torsional vibration test using zebra tapes is the superposition of the dynamic and static angular displacements, with the latter generated because of the varying rotation speed with respect to time. The DSLRL algorithm effectively reduces the phase noise and demodulates the pulse signal phases. The work in this paper provides a method for obtaining reference torsional vibration measurements of rotors based on the zebra-tape method under time-varying speeds.

1. Introduction

The speed of rotation of propellers, aero-engines, or gas turbines fluctuates greatly as they start up, accelerate, decelerate, and stop. The rapidly time-varying rotation speed causes torsional vibration in the rotor shaft. If the instantaneous speed of the rotor reaches the critical torsional speed and remains there for a certain period of time, the excessive torsional vibrations that are produced will seriously threaten the safety of the body. Torsional vibration tests are important means of revealing the variation law of rotor torsional vibration under time-varying speeds.

The zebra-tape method is commonly used to measure rotor torsional vibration [1, 2], as the tapes can be installed on any part of the shaft that is physically accessible [3]. Using noncontact magnetoelectric or eddy sensor with a high-frequency response, the pulse signal is measured as the tapes pass through the sensor probe. By demodulating the pulse

phases and extracting the torsional vibration signal, the torsional vibration can be measured. In this process, pulse phase demodulation is one of the most important tasks, and the accuracy of the phases extracted from the pulse signal directly affects the accuracy of the torsional vibration measurements.

The bending vibration and torsional vibration of machines, nonlinearities in the sensor, and defects in the tape mean that the pulse signal observed by the sensor will not be an ideal square wave or sine wave but will instead feature some modulated frequency, amplitude, and phase components. In addition, the modulated signal will have some interference from the geometric errors inherent in toothed disk structures [4, 5], the electric noise of cable transmission, environmental noise, and so on. All of these factors directly affect the pulse arrival time of the modulated signal, resulting in pulse phase noise [6]. Thus, phase demodulation is a very difficult task in the torsional vibration measurement process.

To date, various phase demodulation methods have been developed, such as the fast Fourier transform [7, 8], Hilbert–Huang transform [9], filtering [10, 11], order tracking filter [12, 13], wavelet decomposition [14], variable mode decomposition [15, 16], and harmonic signal decomposition [17]. These algorithms are mostly based on the theory of frequency domain or time-frequency domain transformation and provide effective torsional vibration phase demodulation with a clear frequency distribution, such as for harmonic components and the geometric errors of toothed disk structures.

For electrical noise and environmental noise, however, although the amplitudes of such noises are very weak relative to the amplitude of the pulse signal, they will cause extreme pulse redundancy. This redundancy makes it very difficult to calculate the pulse duty cycle. Moreover, the phase noise caused by this redundancy is random broad-spectrum noise, so it is difficult to denoise using frequency domain or time-frequency domain algorithms, which seriously affects the accuracy of pulse phase demodulation.

To improve the accuracy of torsional phase demodulation based on zebra tapes under a time-varying rotation speed, this paper derives the relationship between the pulse phase difference of the zebra tapes, the static angular displacement caused by the time-varying rotational speed, and the torsional angular displacement. A phase demodulation algorithm based on downsampling and local resampling (DSLRL) is then proposed. The accuracy of this algorithm is verified through simulation examples of torsional vibration. The algorithm is applied to measure the torsional vibration angle displacement of a propeller shaft under the starting transition process, and the phase demodulation algorithm is further evaluated.

2. Testing Theory

As shown in Figure 1, zebra tapes are installed on the rotating shaft sections, and two noncontact magnetoelectric sensors are used to collect the pulse signals of the tapes passing through the sensors. One of the two sensors is used to observe/measure the phases of torsional vibration, while the other records the reference phases. The signals from the sensors are amplified and adjusted by an acquisition instrument and then transmitted to a computer.

When torsional vibration occurs in the rotor, the time at which the tapes pass the sensors advances or recedes, and this modulates the phases of the test signals. The phase differences (i.e., the advanced or lagged time) caused by phase modulation can be written as

$$\tau(t) = t_\tau(t) - t_0(t). \quad (1)$$

$t_\tau(t)$ is the time at which the pulse extrema (i.e., maxima or minima) are generated by the tapes passing sensor1 under the condition of torsional vibration, and $t_0(t)$ is the time at which the pulse extrema without torsional vibration pass sensor2. We call $t_\tau(t)$ the observation phase and $t_0(t)$ the reference phase; the corresponding signals are called the observation signal and the reference signal.

According to (1), the angular displacement response (in degrees) for the rotor can be expressed as

$$\theta(t) = 360 \times \frac{n(t)}{60} \tau(t) = \theta_\tau(t) - \theta_0(t), \quad (2)$$

$$\theta_\tau(t) = 6n(t)t_\tau(t), \theta_0(t) = 6n(t)t_0(t),$$

where $n(t)$ is the rotation speed of the rotor (rpm). Even if the expressions of $\theta(t)$, $\theta_\tau(t)$, and $\theta_0(t)$ are discretized, (2) shows that $\theta(t)$ can be calculated when the length of $\theta_\tau(t)$ is different from that of $\theta_0(t)$ because of the different zebra tapes, with digital interpolation used to ensure that the data sequences have the same length.

If we consider the variable static angular displacement generated by a time-varying speed, (2) needs to be modified. The modification method is described as follows.

The relationship between the rotor control speed $\bar{n}(t)$ and the static torque $\bar{T}(t)$ applied to the rotor is as follows:

$$\bar{n}(t) = 9549 \frac{P(t)}{\bar{T}(t)} = 9549 \frac{P(t)}{K(\bar{n})\bar{\theta}(t)}, \quad (3)$$

where $P(t)$ is the input power for the rotor and $K(\bar{n})$ is the slowly varying torsional stiffness of the observed shaft segment under the control speed $\bar{n}(t)$ as the gyroscope torque changes with the bending-torsion coupled vibration. (The number 9549 is the conversion coefficient when the speed is in rpm, the power is in kW, and $K(\bar{n})$ is in N·m/°.)

According to (3), the static torsional angle of the rotor is given by

$$\bar{\theta}(t) = 9549 \frac{P(t)}{K(\bar{n})\bar{n}(t)}. \quad (4)$$

It can be inferred from (2) and (4) that the angular displacement of the rotor obtained from the test signals is the superposition of the dynamic and static angular displacements. Thus, (2) can be modified to

$$\theta(t) = \tilde{\theta}(t) + \bar{\theta}(t) = 6n(t)\tau(t), \quad (5)$$

where $\theta^\circ(t)$ is the vibrational angular displacement, which is a high-frequency component compared with the static displacement component $\bar{\theta}(t)$ induced by the time-varying speed.

According to (5), the vibrational angular displacement of the rotor under the time-varying speed is given by

$$\theta^\circ(t) = 6n(t)\tau(t) - \bar{\theta}(t). \quad (6)$$

In practice, it is not necessary to calculate $\bar{\theta}(t)$ with (4) after obtaining the rotor speed $n(t)$ and the phase difference $\tau(t)$, because $\bar{\theta}(t)$ can be determined and eliminated using the trend term decomposition method. Once $\theta(t)$ has been detrended, $\theta^\circ(t)$ can be identified.

3. Phase Demodulation Algorithm

From (1) and (2), determining the angular response of the torsional vibration requires $t_0(t)$ and $t_\tau(t)$, which are the

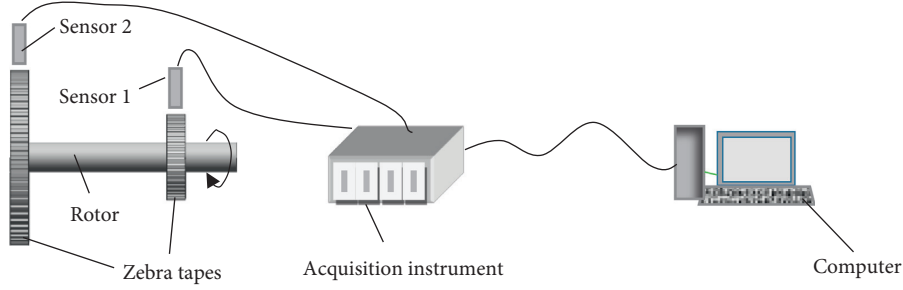


FIGURE 1: Schematic diagram of torsion measuring devices on zebra-tape method.

times of the extrema in the pulse signals. Therefore, an algorithm based on DSLR is constructed to extract the maxima from the pulse signal. First, the upper envelope of the pulse signal is denoised by the downsampling method, and then, the maximum sequence is obtained by locally resampling the original pulse signal. After calculating the angular displacement of the torsional vibration using (6), the phase demodulation of the signals from the two sensors can be realized.

3.1. Denoising the Pulse Phases. We extract the extrema of a pulse signal using a downsampling method to decrease the redundant noise of the extrema.

The interference from weak electrical noise, environmental noise, and step noise makes it difficult to identify the pulse extrema directly using the envelope algorithm or threshold algorithm. The purpose of downsampling is to reduce the occurrence of weak random noises in the pulse signal and avoid redundant extrema, so as to improve the extraction accuracy of pulse phases using more accurate extrema.

Taking phase denoising based on the extraction of maxima as an example, the downsampling pulse phase denoising algorithm is outlined as follows.

Let the signal of the sensor be

$$X = \{X_k = x(t_k) | k = 1, 2, \dots, N\}, \quad (7)$$

where N is the sampling length of signal X .

If the sampling frequency of X is f_s , the maximal testing speed of the rotor is n_{\max} , and the number of tapes is Z , and then, the interval Δk of the downsampling should satisfy the following formula:

$$2 < \Delta k < \left\lfloor \frac{15f_s}{Zn_{\max}} \right\rfloor. \quad (8)$$

The downsampling method resamples data from the original signal every Δk points. The physical meaning of $\lfloor 15f_s / Zn_{\max} \rfloor$ is a quarter of the number of sampling points in one rotation at the maximal test speed ($\lfloor \cdot \rfloor$ represents the rounding down operator). Even if the method decreases the signal sampling frequency, the final sampling frequency is still greater than four times the corresponding frequency of the maximum test speed. Thus, it meets the requirements of the sampling theorem for the digital acquisition of speed pulse signals, and no frequency aliasing will occur.

Downsampling to the sequence X yields

$$\tilde{X} = \left\{ \tilde{X}_i = x(t_1 + i\Delta k) | i = 0, 1, 2, \dots, \left\lfloor \frac{N}{\Delta k} \right\rfloor \right\}. \quad (9)$$

The downsampling process is illustrated in Figure 2. The maximum B is less than the minimum A in Figure 2(a)), so the threshold sampling method cannot be applied to determine the maxima of the signal. Though the accuracy is degraded, the downsampling method can remove weak noise from the signal by decreasing the sampling frequency (Figure 2(b)). The effect is better at larger signal-to-noise ratios or in the case of less noise.

We first look for the maxima of $X^{\%}$ and then search for the maxima of the original signal X near the peaks of $X^{\%}$. The procedure for identifying the peaks of $X^{\%}$ is as follows.

The differential sequence $dX^{\%}$ is obtained as follows:

$$dX^{\%} = \left\{ dX_i^{\%} = X_{i+1}^{\%} - X_i^{\%} | i = 0, 1, 2, \dots, \left\lfloor \frac{N}{\Delta k} \right\rfloor - 1 \right\}. \quad (10)$$

If the i th point in sequence $dX^{\%}$ satisfies

$$\begin{aligned} dX_i^{\%} &> 0, \\ dX_i^{\%} dX_{i+1}^{\%} &\leq 0, \end{aligned} \quad (11)$$

then $X_{i+1}^{\%}$ is the maximum of the downsampling sequence $X^{\%}$. The points that satisfy (11) can be expressed as the sequence

$$\hat{X}_0 = \left\{ X_{i+1}^{\%} | dX_i^{\%} > 0 \text{ and } dX_i^{\%} dX_{i+1}^{\%} \leq 0 \right\}, \quad (12)$$

where \hat{X}_0 is the result of sequence X being downsampled, the physical meaning of which is the upper envelope of the sequence X after being sampled $1/\Delta k$ times. This gives the maxima in the time period $\Delta k/f$. The result of the downsampling method is described in Figure 3, where the triangles denote the components of sequence \hat{X}_0 .

3.2. Extracting the Pulse Phases. \hat{X}_0 is not the maximum sequence of X . To improve the accuracy of the phase calculation and obtain the upper envelope of X , we need to resample X locally.

Let the resampling interval be $2\Delta k$. If $\tilde{X}_{i+1} = x(t_1 + i\Delta k + \Delta k)$ is an element of \hat{X}_0 , the locally resampling sequence is defined by

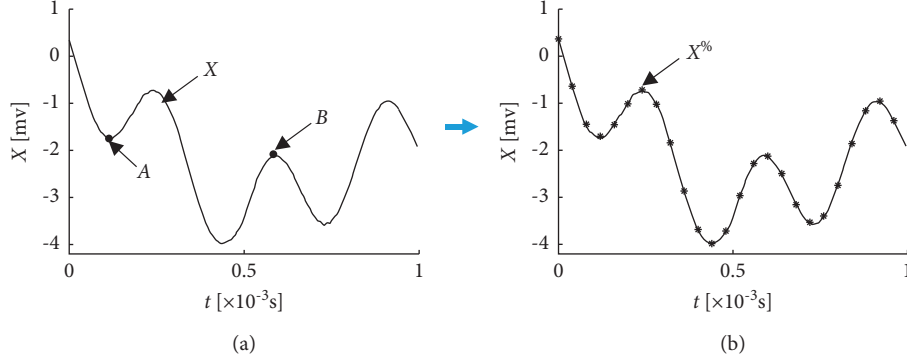


FIGURE 2: Downsampling sequence: (a) the original signal (X) and (b) \tilde{X} in (X).

$$X_{i+1}^L = \{x(t_1 + i\Delta k), x(t_1 + i\Delta k + 1), x(t_1 + i\Delta k + 2), \dots, x(t_1 + i\Delta k + \Delta k), x(t_1 + i\Delta k + \Delta k + 1), x(t_1 + i\Delta k + \Delta k + 2), x(t_1 + i\Delta k + 2\Delta k - 1)\}. \quad (13)$$

The meaning of X_{i+1}^L is illustrated in Figure 4.

The maximum of sequence X_{i+1}^L (Figure 5) can be expressed as

$$\widehat{X}_{i+1} = \max(X_{i+1}^L). \quad (14)$$

Then, the upper envelope sequence of X is given by

$$\widehat{X} = \{\widehat{X}_{i+1}\}. \quad (15)$$

Through this resampling procedure, the maximum sequence \widehat{X} is extracted from X by determining the maxima within $2\Delta k$ of the points in X_0 . This algorithm avoids the interference of weak noise and improves the accuracy of the calculated upper envelope. The upper envelope of the signal X is clarified through (15).

The pulse phases extracted from X are the abscissa sequence \widehat{t} to \widehat{X} in (15), which can be expressed as

$$\widehat{t} = \{\widehat{t}_1, \widehat{t}_2, \dots\}. \quad (16)$$

The physical meaning of DSLR is further illustrated in Figure 6, where the crosses denote extrema that are not peaks in their cycles. These are the redundant points to be denoised.

3.3. Phase Demodulation for Torsional Vibration. Using the DSLR algorithm, the pulse phase sequences \widehat{t}_π and \widehat{t}_0 can be obtained from the observation signal and the reference signal. The phase difference sequence is then calculated as

$$\tau = \{\tau_i = \widehat{t}_{\pi i} - \widehat{t}_{0i} | i = 1, 2, \dots\}. \quad (17)$$

By substituting (17) into (2), the angular displacement response of the rotor is given by

$$\theta = \{\theta_i = 6n_i\tau_i | i = 1, 2, \dots\}, \quad (18)$$

where n_i is the discrete speed, which can be measured experimentally.

Note that θ is a function of time t , but its elements are nonuniform samples after the envelope extraction operation. To obtain the torsional vibration signals at equal time intervals, an interpolation operator must be applied to the sequence θ ; this agrees with Badaoui [18].

According to (6), if only the dynamic vibration signal $\theta^\%$ is needed, the static component $\bar{\theta}(t)$ can be determined using a trending algorithm (e.g., moving average method). This component can then be removed from θ in (18) to obtain a pure vibration signal.

3.4. Phase Demodulation Method. A flowchart of the phase demodulation method for torsional vibration is shown in Figure 7. The proof about the DSLR algorithm is in appendix A.

4. Simulation of the Phase Demodulation of Torsional Vibration

As the focus of this paper is the extraction of the torsional vibration signal, the static torsional angle component caused by the time-varying speed is not considered in the simulation analysis.

The simulation model with a time-varying rotation speed is expressed as

$$\omega(t) = \frac{2\pi}{60}n_1 \sin(0.2\pi t + 2) + 10\pi \cos(0.6\pi t + 0.8) + \frac{2\pi}{60}n_2. \quad (19)$$

Here, the units of ω are rad/s, $n_1 = 1000$ rpm, and $n_2 = 2000$ rpm.

Assume that the number of zebra tapes $Z = 60$. The sampling frequency of the pulse signal is set to $f_s = 200$ kHz and the number of sampling points is $N = 3.5 \times 10^5$ to reduce the distortion of the pulse signal. A frequency of 200 kHz ensures that the number of sampling points on

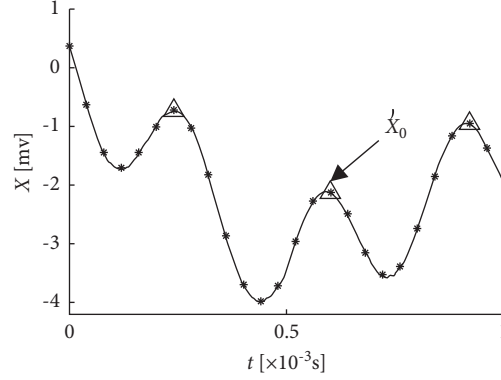


FIGURE 3: Downsampling result.

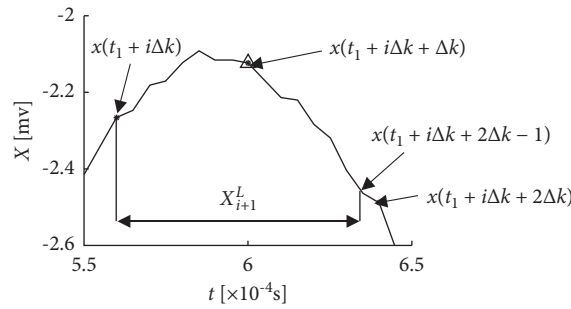


FIGURE 4: Local resampling sequence.

every tape passing the rotation signal is not less than 62 ($2 \times 10^5 / 3200 = 62.5$, where 3200 rpm is the maximum speed). The speed with respect to time is shown in Figure 8.

4.1. Evaluation of Reference Phases. Based on the known time-varying speed, the reference phase $t_0(t)$ can be obtained by the phase demodulation of the sensor signal under the condition of no torsional vibration. At the same time, in the process of estimating the reference phase, the phase denoising and extraction performance of the DSLR method will be verified.

We simulate the reference signal with no torsional vibration as follows:

$$x(t) = \sin Z\omega t + 0.02\eta_1(t), \quad (20)$$

where $\eta_1(t)$ is a uniformly distributed random noise in the interval (0, 1) and t is the uniform speed-up time. The evolution of $x(t)$ in Figure 9 is a harmonic signal with noise, but with no advanced or lagged phase term. Thus, we use $x(t)$ to simulate the reference signal with zero torsional vibration and no phase modulation.

To verify the superiority of the proposed denoising and extraction algorithms, we apply both the DSLR algorithm and the conventional peak-finding algorithm to extract the pulse phases of $x(t)$. According to (8), we set the downsampling interval $\Delta k = 6$ in the DSLR algorithm. The results are shown in Figure 10. The pulse phases extracted by the DSLR method are consistent with the peak values of the original reference signal with no redundancy or omission,

whereas those given by the conventional peak-finding method include the redundant phase points caused by the noise signal. In Figure 10, the stars that do not coincide with the circles are redundant. These redundant points are caused by sensor or environmental noise, and their number and phase are uncertain, which makes it difficult to match the demodulated phase sequence \hat{t}_τ to the reference phase sequence t_0 . This complicates the demodulation of the torsional vibration using (1) or (17). The accuracy of the zebra-tape method is seriously affected by these redundant points.

The reference phase sequence $t_0(t)$ extracted by the DSLR method is shown in Figure 11. The DSLR method is very effective in denoising and extracting the pulse phases.

4.2. Extraction of Torsional Vibration. In this section, we build pulse samples from a torsional sensor and simulate and verify the torsional vibration demodulation algorithm.

Let us assume that the torsional angular displacement signal is as follows:

$$\theta(t) = 2 \sin 64 \pi t. \quad (21)$$

The advance time of the pulse signal caused by torsional vibration is given by

$$\tau(t) = \frac{\pi\theta(t)}{180\omega(t)}. \quad (22)$$

Modulating the phase of $x(t)$ in (20) with $\tau(t)$, the pulse signal of the torsion sensor with noise is given by

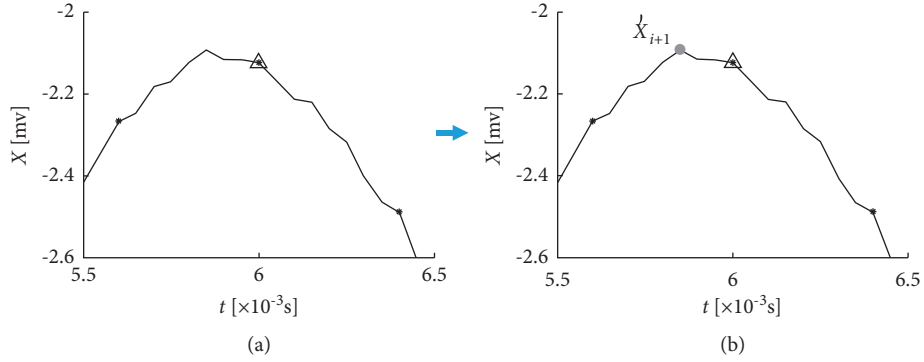


FIGURE 5: Local resampling result: (a) local resampling sequence and (b) the extracted pulse phase point.

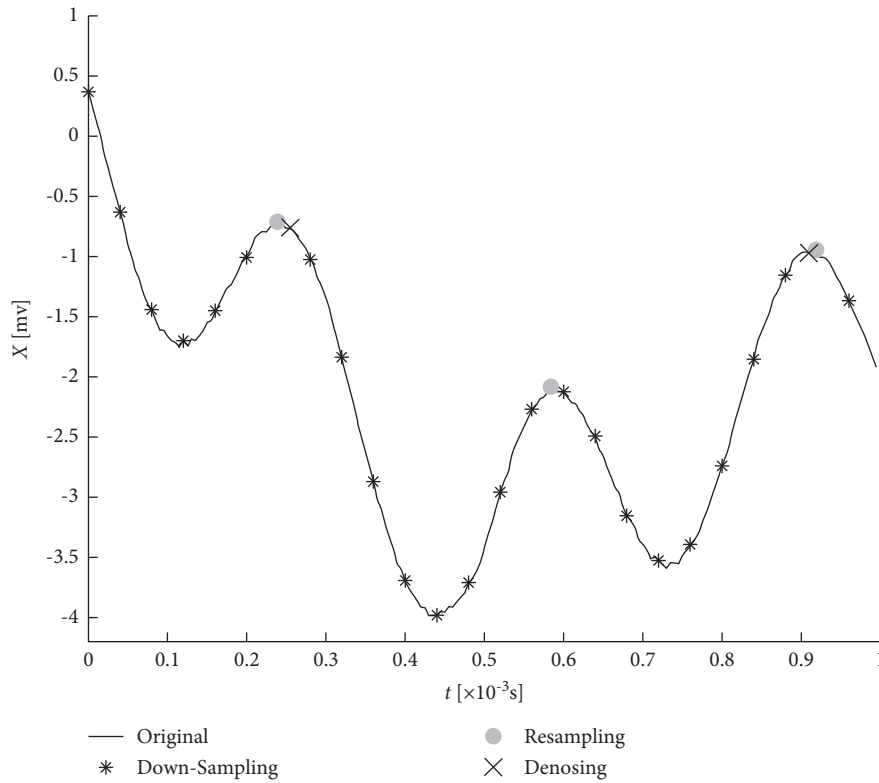


FIGURE 6: The physical meaning of the DSLR phase demodulation algorithm.

$$y(\hat{t}) = \sin Z\omega t + 0.02\eta_2(t), \quad (23)$$

where $\hat{t} = t + \tau(t)$ and $\eta_2(t)$ is uniformly distributed random noise in the interval $(0, 1)$.

Comparing (23) with (20), it can be seen that the variable \hat{t} in (23) is the result of the torsional angular displacement modulation of the variable t in (20). Besides the different sensor noise, the right-hand terms of both equations are consistent, which ensures that $y(\hat{t})$ is the phase modulation result of $x(t)$.

Figure 12 shows the phase difference between the signal pulses with and without torsional vibration. The torsional vibration described by (21) is a constant amplitude, constant frequency harmonic signal. Under the modulation of time-

varying speed, the whole frequency trend of the phase difference $\tau(t)$ decreases with increasing speed, while the amplitude increases.

Figure 13 shows the pulse phases extracted by the DSLR method and the conventional peak-finding method in the presence of torsional vibration. The curve is similar to the calculation result in Figure 10, and the superiority of the proposed algorithm is again apparent.

The modulation phase signal $t_\tau(t)$ obtained by the phase extraction of the modulation signal is shown in Figure 14. This has the same length as the reference phase $t_0(t)$, so we can demodulate the phases of the torsional vibration using (17). The true and calculated torsional signals of the rotor are shown in Figure 15. Compared with the true torsional signal

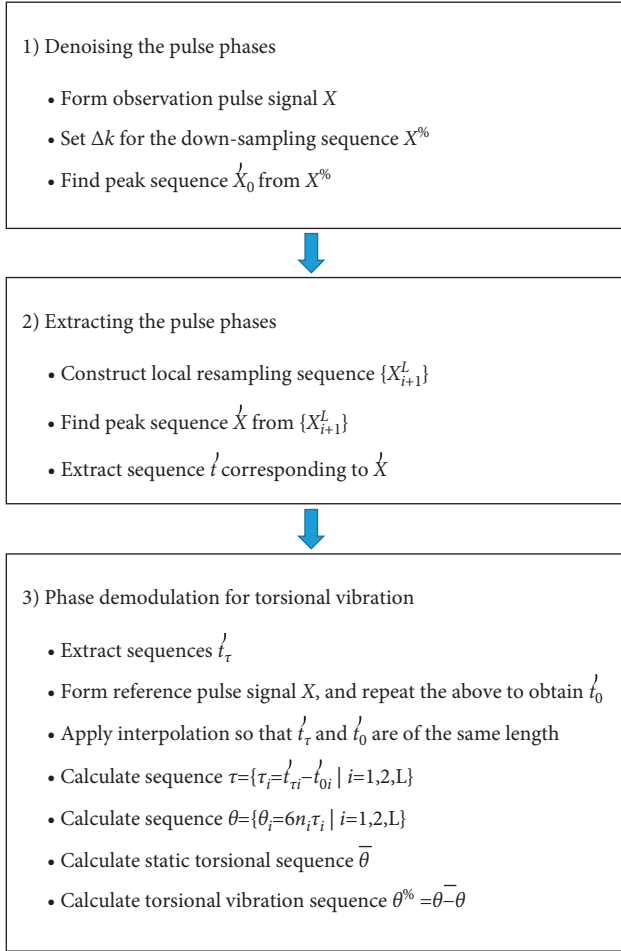


FIGURE 7: Flowchart of phase demodulation algorithm.

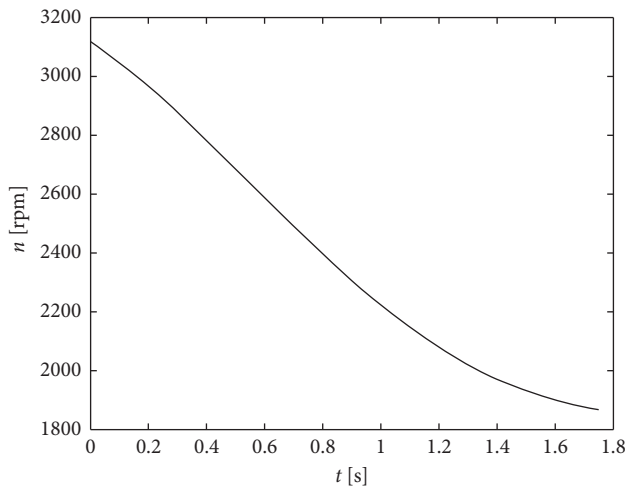


FIGURE 8: The simulation model of time-varying speed.

in Figure 15(a)), the demodulated torsional signal in Figure 15(b) is not distorted in frequency, amplitude, or phase—the largest error in the amplitude is only 1.3%, which verifies the correctness and high accuracy of the proposed DSLR algorithm for the demodulation of torsional vibration.

5. Torsional Vibration Test of a Propeller Shaft

The torsional vibration of a civil aircraft propeller shaft was measured under the start-up condition. Figure 16 shows the test devices used to induce torsional vibration in the propeller shaft. The speed controller adjusted the speed of the engine according to the output power. A reducer with a reduction ratio of 1.69 allowed the engine to rotate the propeller. Zebra tapes were installed on the input shaft of the propeller, and two magnetoelectric sensors were used to collect the torsional vibration signals. One sensor recorded the passing pulses from the zebra tapes on the propeller shaft, the signal of which was used to determine the observation phases of torsional vibration. The other sensor recorded the passing pulses from the toothed disk on the engine rotor, the signal of which was used to determine the reference phases. The pulse signals from both sensors were output to an acquisition conditioner before being sent to a computer.

The zebra tapes were machined specially from 0.2-mm-thick metal material for the test. First, 60 uniform zebra tapes were glued on the input shaft of the propeller. The tapes at 0° and 180° in the circumferential direction were then torn off to provide a rotation speed flag and for rotor balance. The disk controlling the engine speed had 60 teeth, but the zebra tape at 0° was removed for the speed test. A torsional spring was installed at the connection between the toothed disk and the shaft of the engine rotor, so as to weaken the influence of shaft torsion and improve the accuracy of the engine speed measurements. The toothless disk and the torsional spring are original components of the engine rotor itself rather than added for this torsional vibration test.

The time-varying speed of the propeller shaft at a signal sampling frequency of $f_s = 216$ kHz is shown in Figure 17. The speed of the propeller shaft climbed slowly from 1200 rpm with some slight fluctuations up to 28 s and then entered the fast nonuniform climbing stage. The signals of the test sensors are shown in Figures 18 and 19. Figure 18 shows that the output voltage of the propeller sensor increased continuously, indicating some bending vibration on the input shaft of the propeller. The missing tapes modulated the amplitude, frequency, and phase of the observation signal of the propeller shaft, as shown in Figure 19.

The reference signals from the engine rotor are shown in Figure 20 and 21. Comparing Figure 19 with Figure 21, it can be seen that the number of missing zebra tapes on the propeller shaft is twice that of the toothed disk, which is consistent with the actual working condition. The torsional spring ensures that highly accurate reference phases can be obtained by demodulating the signal in Figure 21.

Using the DSLR algorithm, we demodulated the pulse signals in Figures 18 and 20 to obtain $t_\tau(t)$ and $t_0(t)$ in turn. From formula (2) and the speed signal in Figure 17, we obtain $\theta_\tau(t)$ and $\theta_0(t)$, respectively; the speed signal to calculate $\theta_0(t)$, especially, was 1.69 times that in Figure 17.

However, the lengths of discrete $\theta_\tau(t)$ and discrete $\theta_0(t)$ were unequal, because of the different speeds of the propeller and the engine rotor leading both pulse signals had

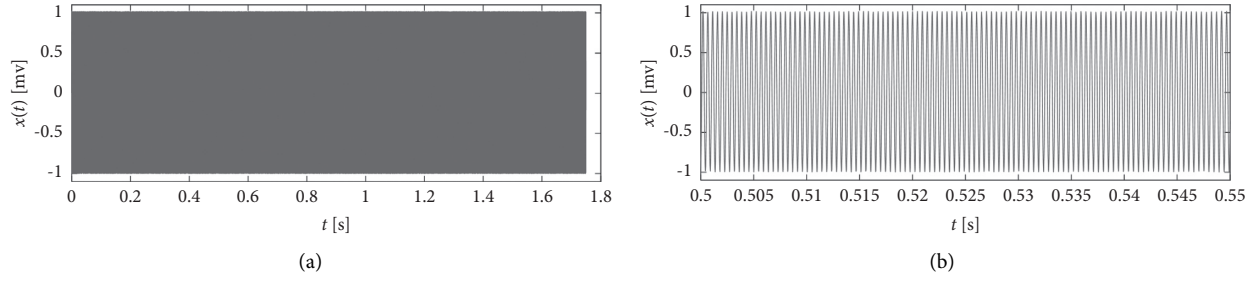


FIGURE 9: The pulse signal of nontorsional vibration: (a) $x(t)$ and (b) the local amplification of $x(t)$.

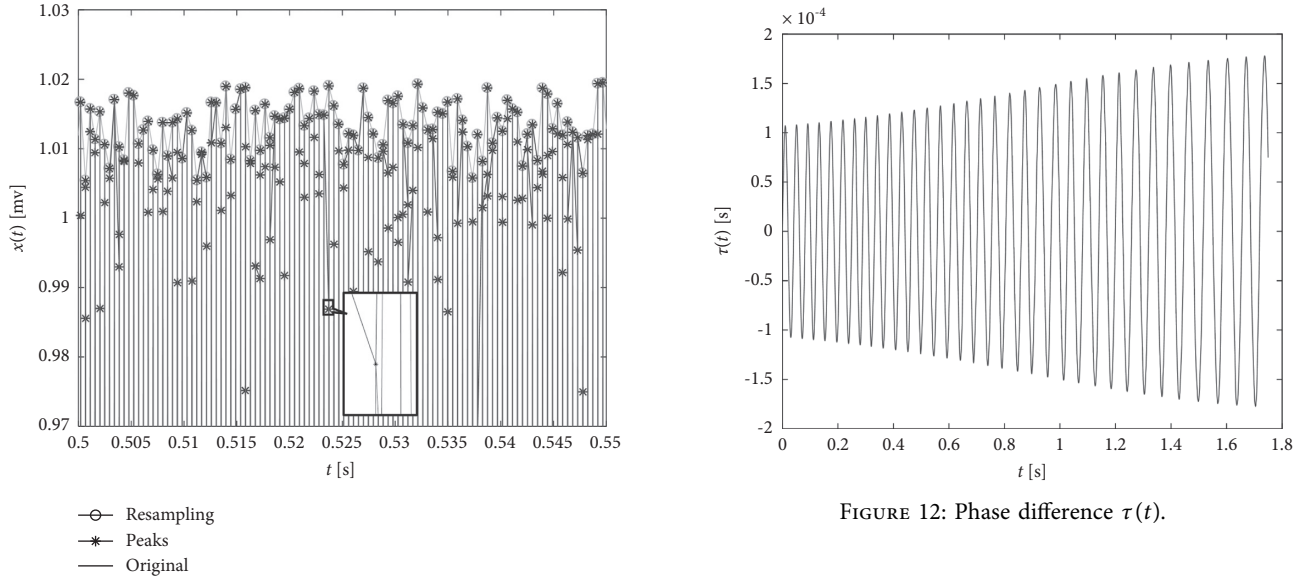


FIGURE 12: Phase difference $\tau(t)$.

FIGURE 10: Comparison of DSLR and find-peaks methods on $t_0(t)$.

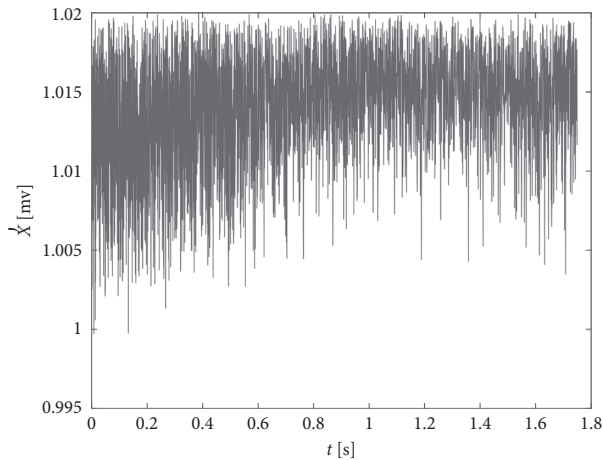


FIGURE 11: Reference phase $t_0(t)$.

different pulse numbers, we cannot use formula (2) to calculate $\theta(t)$ directly.

Given the reduction ratio is 1.69, the length of discrete $\theta_0(t)$ is 1.69 times that of $\theta_\tau(t)$; thus, an operator about linear interpolation to $\theta_0(t)$ was done to make the lengths of discrete $\theta_\tau(t)$ and discrete $\theta_0(t)$ equal, and then, formula (2)

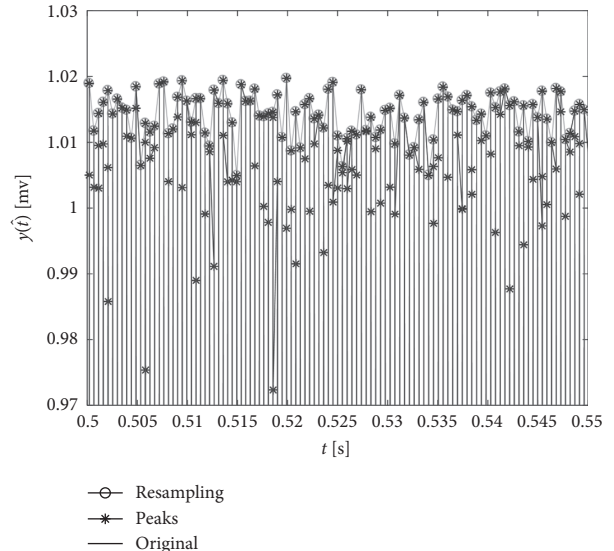


FIGURE 13: Comparison of DSLR and find-peaks methods on $t_\tau(t)$.

was used to calculate torsional vibration $\theta(t)$. The final demodulated torsional vibration signal is shown in Figure 22.

The propeller shaft exhibited slowly varying static torsional displacement as the speed changes with time, and it

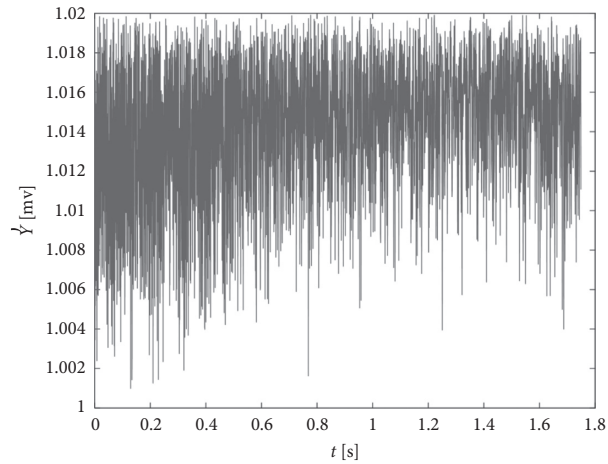


FIGURE 14: Modulated phases $t_r(t)$.

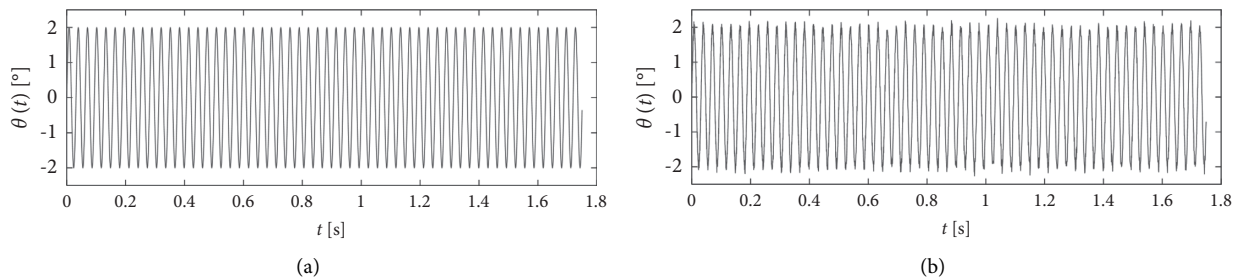


FIGURE 15: Results of torsional vibration angle: (a) actual and (b) calculated.

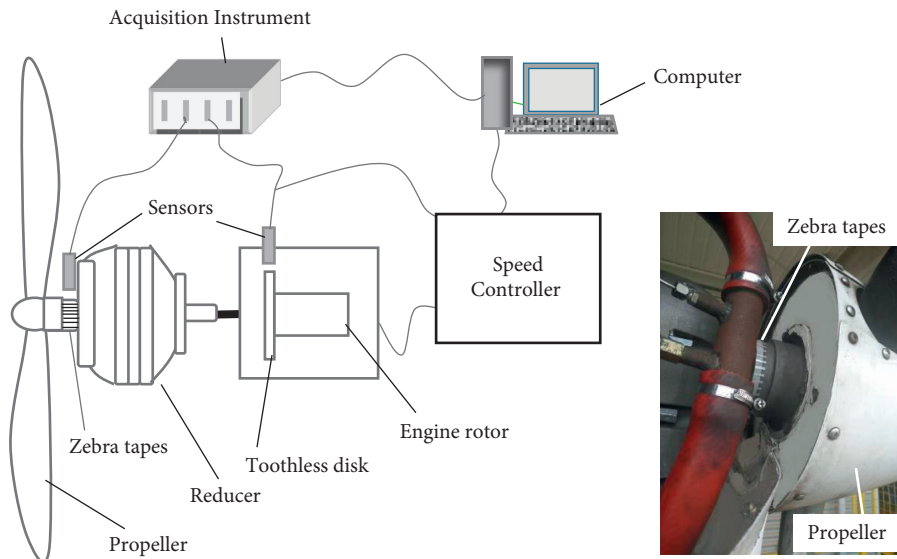


FIGURE 16: The torsional vibration test apparatus.

was speculated that the reason introducing the static term is shown in formula (3). The torsional displacement displayed a downward trend as the speed increases. The possible reason was that the running power of the propeller gradually matched the power output to it by the engine, which reduced the torsional vibration.

Applying the detrending operator to the demodulated signal in Figure 22 not only removes the influence of static torsional displacement caused by time-varying speed but also weakens the interference noise caused by the missing zebra tapes. The torsional vibration angles of the propeller shaft with respect to time and speed are shown in Figures 23

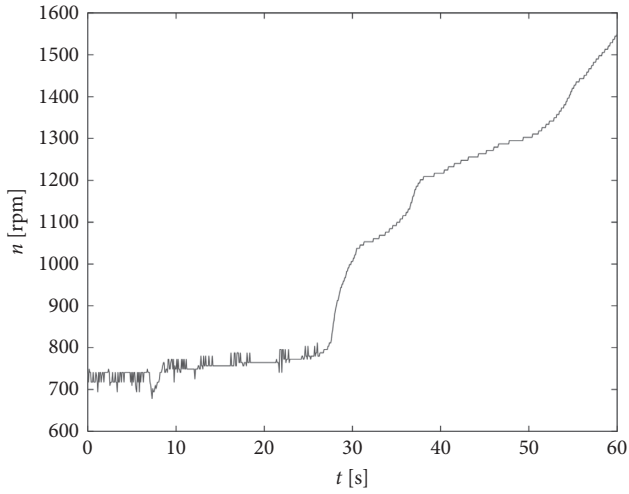


FIGURE 17: Time-varying speed of a propeller shaft.

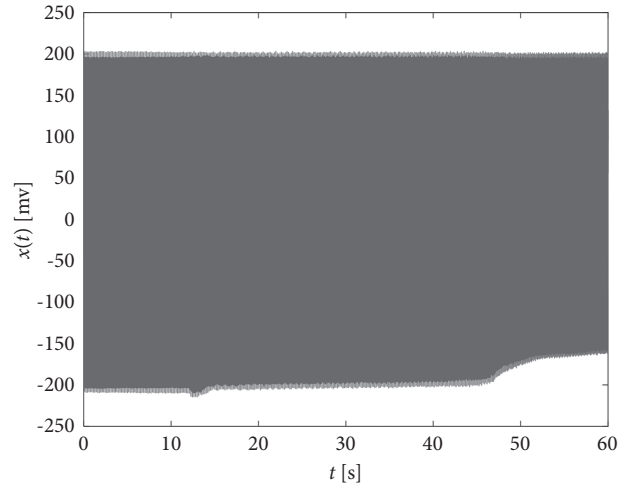


FIGURE 20: Reference signal from the engine rotor.

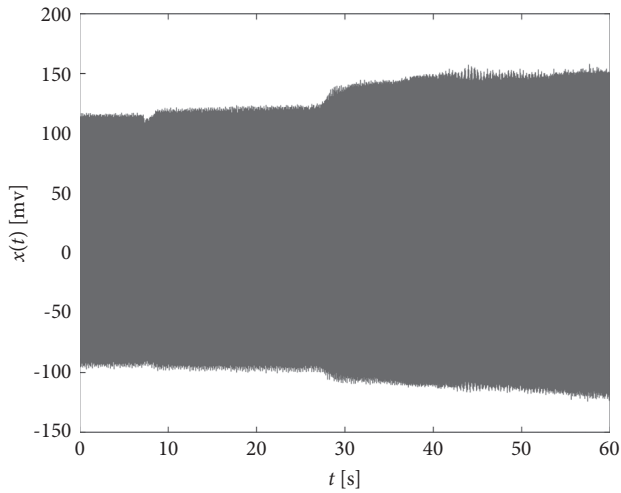


FIGURE 18: Observation signal of the propeller shaft.

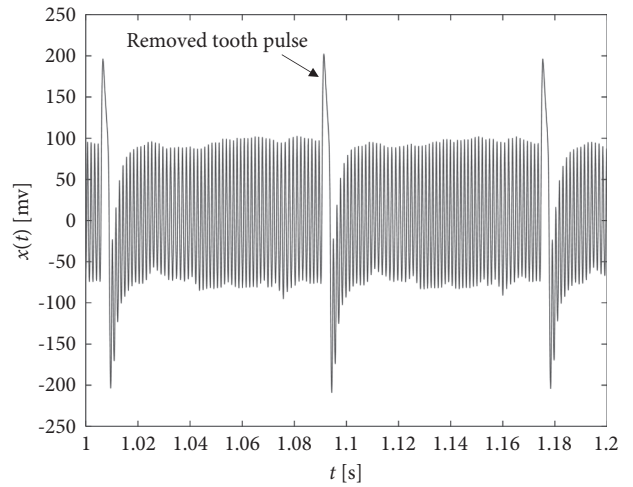


FIGURE 21: Amplified reference signal.

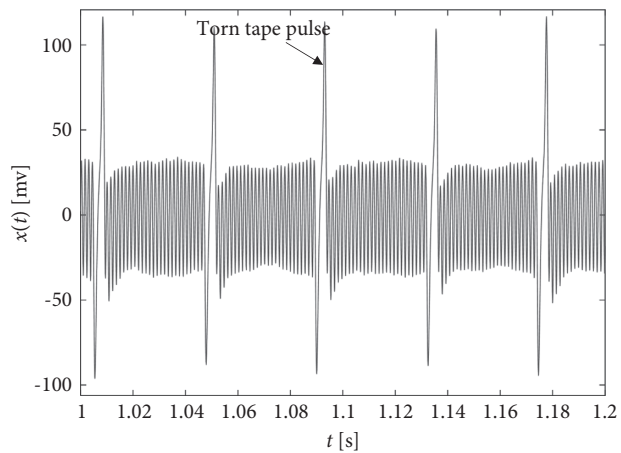


FIGURE 19: Amplified observation signal of the propeller shaft.

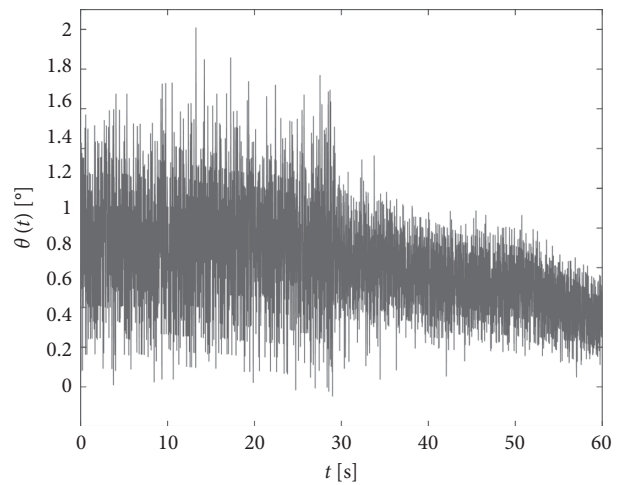


FIGURE 22: Torsional angle with static torsion effect of the propeller shaft.

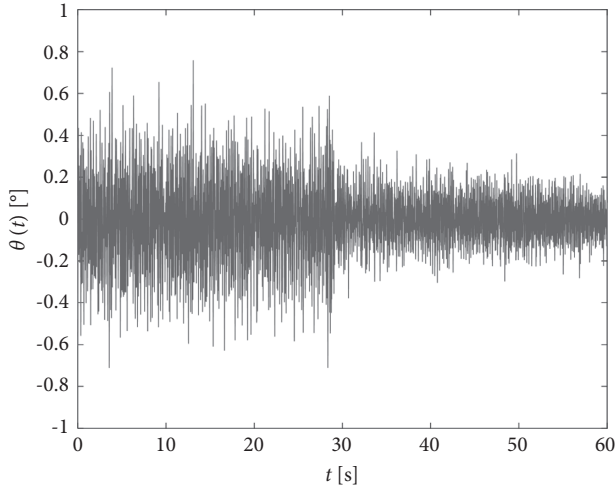


FIGURE 23: vibration angle vs. time of the propeller shaft.

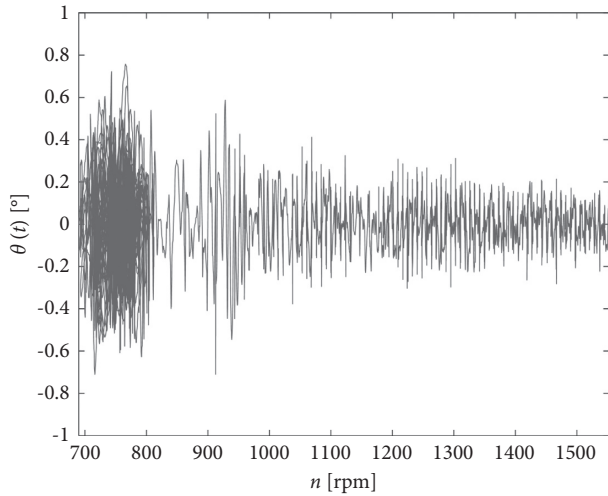


FIGURE 24: Vibration angle vs. rotation speed of the propeller shaft.

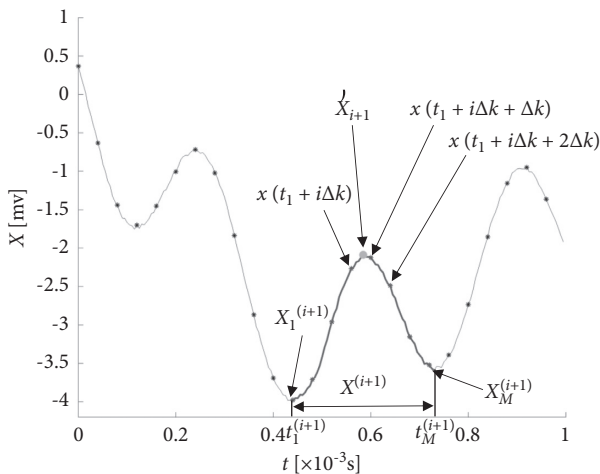


FIGURE 25: A pulse signal cycle $X^{(i+1)}$.

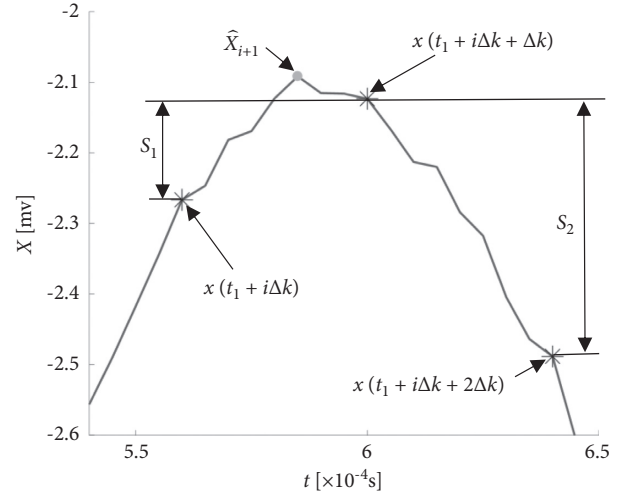


FIGURE 26: The illustration of the set (S).

and 24. The torsional vibration of the propeller shaft decreases with speed, and reaches a maximum value at 770 rpm. Contrasting this with Figure 17, it appears that the torsional vibration response decreases as the speed changes rapidly from 800 rpm to 900 rpm, which indicates that the torsional vibration of the rotor is suppressed to a certain extent when the instantaneous speed becomes too fast. When the propeller shaft speed exceeds 900 rpm, although the propeller speed still increases rapidly, the torsional vibration response also increases. This indicates that the relationship between the time-varying speed and the torsional vibration response is nonlinear, and the time-varying speed is not the main factor affecting the torsional vibration of the rotor. Specifically, the shapes of the curves in Figure 24 before 800 rpm are caused by the slight jitter of the rotation speed.

6. Conclusion

To extract the torsional angular displacement from pulse signals, this paper has proposed the DSLR phase demodulation algorithm and described its application to a working propeller shaft. Experiments were conducted in which the static angular displacement was considered in a torsional vibration test for a rotor with a time-varying speed based on the zebra-tape method.

Under the condition of a time-varying rotational speed, the angular displacement obtained by the zebra-tape method was found to be the superposition of dynamic and static torsional angular displacements. After removing the static angular displacement component, the remaining torsional vibration signal is proportional to the rotation speed with some phase difference. The calculation of the phase difference is dependent on the phase of the observation signal and the reference phase.

For a rotor torsional vibration pulse signal with time-varying speed and weak noise, the secondary sampling of the pulse signal based on DSLR can improve the demodulation accuracy of the torsional vibration phases.

When the instantaneous rotation speed is too high, the torsional vibration response amplitude of the rotor is inhibited, but this is not always the most important factor affecting the torsional vibration response amplitude of the rotor.

Appendix

The proof of the denoising feature about the DSLR algorithm

In this appendix, the denoising feature of the DSLR theory will be proved. The proof is divided into two parts:

- (1) \widehat{X} is the upper envelop sequence of X .
- (2) \widehat{X} is the denoised upper envelop sequence of X .

First, the authors prove \widehat{X} is the upper envelop sequence of X .

Proof. We extract any pulse signal cycle $X^{(i+1)}$ from X as the signal in Figure 25; it satisfies $\widehat{X}_{i+1} \in X^{(i+1)}$ and

$$X^{(i+1)} = \{X_r^{(i+1)} = x(t_r^{(i+1)}) | r = 1, 2, \dots, M\}. \quad (\text{A.1})$$

Because the time-varying speed and other factors (e.g., toothless disk), $X^{(i+1)}$ is an asymmetric harmonic signal, where both the first and the last points are valley values. And the points with star symbol are the downsampling points. The purpose of this extracting is to prove the problem more easily.

From formulas (12)–(14), the authors can know $\widehat{X}_{i+1} \geq x(t_1 + i\Delta k + \Delta k)$. Since

$$\begin{aligned} x(t_1 + i\Delta k + \Delta k) &> x(t_1 + i\Delta k), \\ x(t_1 + i\Delta k + \Delta k) &> x(t_1 + i\Delta k + 2\Delta k). \end{aligned} \quad (\text{A.2})$$

Thus,

$$\widehat{X}_{i+1} > x(t) \quad t \in [t_1^{(i+1)}, t_1 + i\Delta k] \cup [t_1 + i\Delta k + 2\Delta k, t_M^{(i+1)}]. \quad (\text{A.3})$$

On the other hand, from formula (14), the authors can know

$$\widehat{X}_{i+1} = \max\{x(t) | t \in [t_1 + i\Delta k, t_1 + i\Delta k + 2\Delta k]\}. \quad (\text{A.4})$$

So, $\widehat{X}_{i+1} = \max\{x(t) | t \in [t_1^{(i+1)}, t_M^{(i+1)}]\}$.

Therefore, \widehat{X} is the upper envelop sequence of X . \square

Second, the authors prove \widehat{X} is the denoised upper envelop sequence of X . \square

Proof. We still select the above $X^{(i+1)}$ to prove this problem. The noise sequence superposed in $X^{(i+1)}$ is expressed as

$$H_r^{(i+1)} = \{H_r^{(i+1)} = \eta(t_r^{(i+1)}) \quad | r = 1, 2, \dots, M\}. \quad (\text{A.5})$$

To noises in the time domain $[t_1^{(i+1)}, t_1 + i\Delta k] \cup [t_1 + i\Delta k + 2\Delta k, t_M^{(i+1)}]$, that is,

$$H_r^{(i+1)} \in \{\eta(t) | t \in [(t_1^{(i+1)}, t_1 + i\Delta k)] \cup [t_1 + i\Delta k + 2\Delta k, t_M^{(i+1)}]\}. \quad (\text{A.6})$$

From the locally resampling theory and Figure 25, we can know the noises happened in formula (A.6) do not participant in the maximum calculation, so the noises in this domain are denoised fully.

To the noises in the time domain $(t_1 + i\Delta k, t_1 + i\Delta k + 2\Delta k)$, that is,

$$H_r^{(i+1)} \in \{\eta(t) | t = (t_1 + i\Delta k, t_1 + i\Delta k + 2\Delta k)\}. \quad (\text{A.7})$$

Define a set $S \in X^{(i+1)}$ by

$$S = \{x(t) | x(t) < x(t_1 + i\Delta k + \Delta k) \& t \in (t_1 + i\Delta k, t_1 + i\Delta k + 2\Delta k)\}. \quad (\text{A.8})$$

The definition of A is further illustrated in Figure 26, where

$$S = S_1 \cup S_2,$$

$$S_1 = \{x(t) < x(t_1 + i\Delta k + \Delta k) | t \in (t_1 + i\Delta k, t_1 + i\Delta k + \Delta k)\}, \quad (\text{A.9})$$

$$S_2 = \{x(t) < x(t_1 + i\Delta k + \Delta k) | t \in [(t_1 + i\Delta k + \Delta k, t_1 + i\Delta k + 2\Delta k)\}.$$

From the locally resampling theory, $x(t_1 + i\Delta k + \Delta k)$ is an element of \widehat{X}_0 and \widehat{X}_0 is a maximum sequence in the down-sampling set $X^{\%}$. Thus, if noises superposed in S satisfy

$$\begin{aligned} H_r^{(i+1)} &> x(t_1 + i\Delta k + \Delta k) - x(t_1 + i\Delta k), \\ \text{or} & \\ H_r^{(i+1)} &> x(t_1 + i\Delta k + \Delta k) - x(t_1 + i\Delta k + 2\Delta k), \end{aligned} \quad (\text{A.10})$$

they will be denoised.

At the same time, because \widehat{X}_{i+1} is the only maximum remained in the time segment $(t_1 + i\Delta k, t_1 + i\Delta k + 2\Delta k)$, the other extreme noises are denoised too. According to the previously mentioned analysis, the noises in the time domain $(t_1 + i\Delta k, t_1 + i\Delta k + 2\Delta k)$ can be denoised partially.

So, the DSLR algorithm has the denoising feature to $X^{(i+1)}$.

Therefore, the fact that \widehat{X} is the denoised upper envelop sequence of X is proved. \square

Data Availability

The data that support the findings of this study are available on request from the corresponding author.

Conflicts of Interest

The authors declare that there are no conflicts of interest regarding the publication of this paper.

Acknowledgments

This research was supported by National Science and Technology Major Project (2017-IV-0008-0045).

References

- [1] W. Dou, N. Zhang, and Z. S. Liu, "The coupled bending and torsional vibrations of the high-speed geared rotor-bearing system," *Journal of Vibration Engineering*, vol. 24, no. 4, pp. 385–393, 2011.
- [2] Y. F. Jiang, M. F. Liao, and S. J. Wang, "New measuring method for torsion vibration of aeroengine rotor," *Journal of Vibration, Measurement & Diagnosis*, vol. 33, no. 3, pp. 410–416, 2013.
- [3] H. Luo, R. Chumai, N. Peton, and A. Menoin, "Torsional vibration detection using high sampling rate and high resolution Keyphasor information," in *Proceedings of the ASME International Design Engineering Technical Conference and Computers and Information in Engineering Conference*, Portland, OR, USA, August 2013.
- [4] C. L. Groover and M. W. Trethewey, "Removal of order domain content in rotating equipment signals by double resampling," *Mechanical Systems and Signal Processing*, vol. 19, no. 3, pp. 483–500, 2005.
- [5] J. Liska, J. Jakl, and S. Kunkel, "Measurement and evaluation of shaft torsional vibrations using shaft instantaneous angular velocity," *Journal of Engineering for Gas Turbines & Power*, vol. 141, no. 4, pp. 041029.1–041029.5, 2019.
- [6] D. D. Yan and L. Yue, "Shaft torsional vibration measuring technique for rotor system based on zebra strip," *Mach Build Auto*, vol. 49, no. 4, pp. 202–205, 2020.
- [7] T. Tsuji, H. Fujiwara, and O. Matsushita, "Vibration of bending-torsion coupled resonance in a rotor," in *Proceedings of the ASME International Design Engineering Technical Conference and Computers and Information in Engineering Conference*, Portland, OR, USA, August 2013.
- [8] P. Borghesani, P. Pennacchi, and S. Chatterton, "The velocity synchronous discrete Fourier transform for order tracking in the field of rotating machinery," *Mechanical Systems and Signal Processing*, vol. 44, pp. 118–133, 2013.
- [9] D. Q. Ren, Z. T. Wu, and S. X. Yang, "Research on an estimate method of torsional vibration for rotating machinery based on HHT analysis," *Turbine Technology*, vol. 47, no. 6, pp. 430–432, 2005.
- [10] D. H. Diamond, P. S. Heyns, and A. J. Oberholster, "Online shaft encoder geometry compensation for arbitrary shaft speed profiles using Bayesian regression," *Mechanical Systems and Signal Processing*, vol. 81, pp. 402–418, 2016.
- [11] D. Rémond, J. Antoni, and R. B. Randall, "Instantaneous Angular Speed (IAS) processing and related angular applications," *Mechanical Systems and Signal Processing*, vol. 45, pp. 24–27, 2014.
- [12] M. D. Coats and R. B. Randall, "Single and multi-stage phase demodulation based order-tracking," *Mechanical Systems and Signal Processing*, vol. 44, no. 1-2, pp. 86–117, 2014.
- [13] M. Zhao, J. Lin, X. Wang, Y. Lei, and J. Cao, "A tachometerless order tracking technique for large speed variations," *Mechanical Systems and Signal Processing*, vol. 40, no. 1, pp. 76–90, 2013.
- [14] X. H. Sun, X. W. Dong, and M. M. Hao, "Research on testing method of torsional vibration based on wavelet ridge extraction," *Journal of Vibration, Measurement & Diagnosis*, vol. 40, no. 1, pp. 135–140, 2020.
- [15] S. Braut, R. Žigulić, and A. Skoblar, "Fault Detection Based on Instantaneous Angular Speed Measurement and Vibrational Mode Decomposition," in *Proceedings of the Matec Web of Conferences*, p. 211, Guangzhou, China, July 2018.
- [16] S. Braut, R. Iguli, and A. Skoblar, "Partial rub detection based on instantaneous angular speed measurement and vibrational mode decomposition," *Journal of Vibration Engineering Technol.*, vol. 8, no. 2, pp. 351–364, 2020.
- [17] K. Rodopoulos, C. Yiakopoulos, and I. Antoniadis, "A parametric approach for the estimation of the instantaneous speed of rotating machinery," *Mechanical Systems and Signal Processing*, vol. 44, no. 1-2, pp. 31–46, 2014.
- [18] M. El Badaoui and F. Bonnardot, "Impact of the non-uniform angular sampling on mechanical signals," *Mechanical Systems and Signal Processing*, vol. 44, no. 1-2, pp. 199–210, 2014.